1-1-2010

Prediction Of Optical Properties Of Plasmonic Composites: Applications To Solar Energy Harvesting

Satvik Wani

Recommended Citation

Wani, Satvik, "Prediction Of Optical Properties Of Plasmonic Composites: Applications To Solar Energy Harvesting" (2010). *All Theses and Dissertations (ETDs)*. 830.
https://openscholarship.wustl.edu/etd/830

WASHINGTON UNIVERSITY IN ST. LOUIS

School of Engineering and Applied Science

Department of Energy, Environmental and Chemical Engineering

Thesis Examination Committee:

Radhakrishna Sureshkumar, Chair

Yinjie Tang

Palghat Ramachandran

PREDICTION OF OPTICAL PROPERTIES OF PLASMONIC COMPOSITES:

APPLICATIONS TO SOLAR ENERGY HARVESTING

by

Satvik Navinbhai Wani

A thesis presented to the School of Engineering
of Washington University in partial fulfillment of the
requirements for the degree of

MASTER OF SCIENCE

August 2010
Saint Louis, Missouri

ABSTRACT OF THE THESIS

Prediction of Optical Properties of Plasmonic Composites:

Applications to Solar Energy Harvesting

by

Satvik Navinbhai Wani

Master of Science in Energy, Environmental and Chemical Engineering

Washington University in St. Louis, 2010

Research Advisor: Professor Radhakrishna Sureshkumar

The finite difference time domain method was used to simulate the optical response of plasmonic composites with one and two nanoscale spherical metallic inclusion(s) (Ag/Cu in Air/SiO$_2$) with various diameters and compositions. Fair agreement was found between simulation and effective medium theories for binary and ternary composites. Responses of ternary Ag/Cu/ SiO$_2$ composites with various Ag:Cu ratios were found to be in fair agreement with the experimental data obtained from literature. Experiments with photosynthetic microalga *Chlamydomonas Reinhardtii* and *Cyanothece* showed that the wavelength specific backscattering in the blue region of the spectrum from an Ag nanoparticle suspension could promote microalgal growth by more than 30%. This was because the photoactivity of green microalgae is non-monotonic across the electromagnetic spectrum. The wavelength and light flux of the backscattered field were found to be controllable through the variation of the geometric features and/or concentration of the nanoparticles in the suspension.

Acknowledgments

Satvik Navinbhai Wani

Washington University in St. Louis
August 2010

Contents

List of Figures

Chapter 1

Introduction

1.1   Motivation

Efforts to realize the implementation of the idea of a "solar economy" are at their fullest in today's world. Processing, materials and installation costs of solar energy harvesting methods are some of the major concerns [1]. Naturally, maximization of the operating efficiency of a solar unit is very important. Out of the various methodologies that are being explored today, plasmonics based efficiency enhancement techniques have shown promising results, especially in the case of photovoltaic (PV) devices [1]. The philosophy behind this is can be summarized in the following manner. While one way to improve the efficiency of PV devices is to use materials different form silicon based materials, such materials come with a set of challenges mainly in the form of development of the processing technology, optimization of processing cost, materials cost etc. Another way is to explore the use of well established materials and technologies with a set of enhancing modifications that do not add significant process and materials technology development transition costs. As summarized by Atwater et al. in Ref. [1], plasmonics based enhancement in PV devices generally require adding noble metal nanoparticles on or in existing device architectures. This retrofitting simplicity makes application of plasmonics to solar energy harvesting a very attractive candidate for the future of solar technologies.

Plasmonics concerns itself with the fundamental study and utilization of the interaction of light with electron plasma (typically in noble metals) at the nanoscale [2]. A plasmon is the quantized version of these plasma waves. It is possible to excite plasmons by light in a metal at a metal-dielectric interface. These electron density waves near the surface in the metal are called surface plasmons. In case surface plasmons are excited on isolated nanostructures embedded in a dielectric, they are called localized surface plasmons. The electron plasma and the incident electromagnetic field form a damped oscillator like system for low intensities of radiation. Here, the attractive Coulombic force acting on displaced electrons can be seen as the restoring force and the resistivity of the metal causes the damping. Hence, a resonance condition exists for a particular system. Resonance occurs at $\min(\varepsilon_p + 2\varepsilon_m)$ where ε_p is the permittivity of the spherical metallic particle and ε_m is the permittivity of the medium [2],[3]. This resonance occurs at visible wavelengths of light typically for noble metals like Au and Ag. This makes them viable candidates for enhancing the light harvesting efficiency of solar devices in the visible range of the electromagnetic spectrum.

Fig. 1.1 shows the spatial distribution of the logarithm of the Poynting vector magnitude $\log_{10}|\mathbf{S}|$ at resonance wavelength $\lambda = 392\,\mathrm{nm}$ (fig 1.1a) and at off-resonance wavelength $\lambda = 400\,\mathrm{nm}$ (fig. 1.1b) for a 10 nm diameter Ag nanoparticle in air. Notice the reduction in concentration of radiant flux at the off-resonant wavelength. This concentrated radiant flux can be funneled into an active PV device by placing such nanoparticles (NPs) on or into the device [1],[4]. Further, as discussed in chapter 4, plasmonic NP suspensions can be used as wavelength specific backscattering devices for promoting functional microalgae growth.
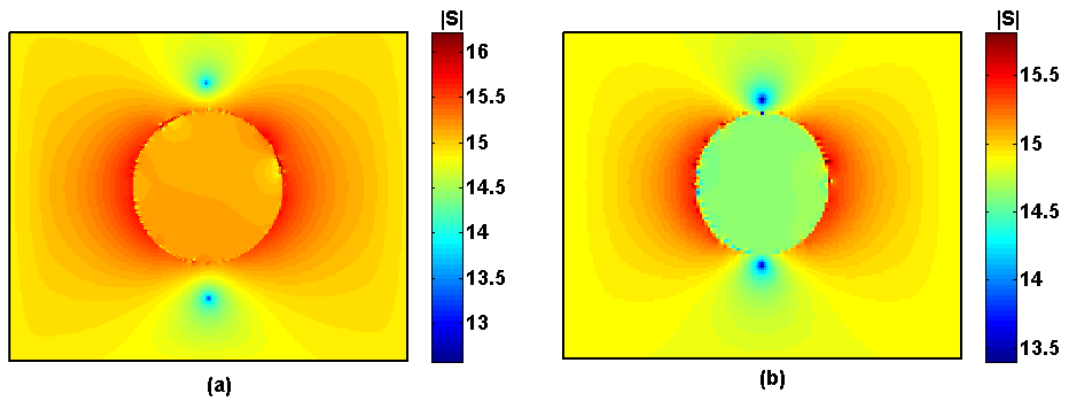
Figure 1.1: Spatial distribution of Poynting vector S on a logarithmic scale for a 10 nm diameter spherical Ag nanoparticle in air at (a) resonant wavelength (392 nm) and (b) off-resonant wavelength (400 nm.) FDTD simulation were done with an input power of 1 W/m^2.

A more general approach to utilization of plasmon based enhancement for solar energy harvesting has been proposed by Trice et al. [5]. The central idea was that plasmonic composites can be thought of as solar energy harvesting devices by themselves owing to the enhanced plasmon based absorption. They have also discussed design rules for such composites based on existing simple mixing rules and their extensions proposed by Garcia et al. [6]. Further, it was shown that multiple metal composites can utilize the combination of individual resonant responses to absorb in a broad range of the solar spectrum and hence, may be thought of as broadband solar antennae. This was the starting point of the current work.

1.2 Objectives and Problem Formulation

Solar electromagnetic (EM) radiation, in principle, is one of the few uninterruptible sources of energy that is readily accessible. The most general way to capture this radiant flux is through interception by an absorbing object. Any passive object placed in the path of radiation interacts with it in two ways:

- *Absorption A*: Some intercepted radiant power is absorbed into the *mass m* of the object.

- *Scattering S*: Some power is deflected as a result of interaction with the object. For large enough objects, this can be subdivided into *Reflection R* and *Transmission T*, especially for slab like geometries.

This translates to: $S + A = 1$ or $R + T + A = 1$. Efficient harvesting of solar radiant energy is then primarily governed by the following:

- *Maximization of absorption* in the intercepting object.

- *Minimization of the mass* of the intercepting object.

The last point takes economics into consideration. Therefore, a Solar Energy Harvester (SEH) can be defined as any device which can absorb solar radiant energy. A simple figure of merit φ for a SEH can, then, be defined as:

$$\varphi = \frac{1}{m}\left(\frac{A}{S}\right).$$

(1.1)

4

A perfect SEH would have: $\varphi \rightarrow \infty$. This is a very basic definition. A more rigorous figure of merit should take into account the aspect of utilization/conversion of the absorbed power. This is outside the scope of the present study.

Ray optics can be applied to objects that are much larger than the wavelength of the incident radiation. In order to maximize interception, an object's surface must be perpendicular to the incident radiation. Solar radiation is primarily made up of parallel beams [7]. Hence a SEH should ideally be an object with least possible mass and largest flat surface. This, naturally, means that thin-films are the ideal candidates.

Objects comparable to or smaller than the wavelength of incident radiation do not follow ray optics because of diffraction [3],[8]. In this case, interception can be quantified by the absorption and scattering cross-sections of the object. These cross-sections are complex functions of the object's structure, size, surroundings and composition. Therefore, unlike the previously discussed case, it is impossible to choose the ideal structure based on purely geometrical arguments [3].

Scattering and reflection occur at an interface where the refractive index is spatially discontinuous [8]. We neglect the case of objects that are small compared to the wavelength of light for reasons discussed previously. Then, for the case of a thin-film SEH, scattering/reflection can be reduced if there are no spatial discontinuities in the refractive index at the surrounding medium and SEH interface. Schubert et al. have shown that graded refractive index SiO_2/TiO_2 films can be used to practically eliminate Fresnel reflection from

AlN substrates [9]. Similarly materials with graded real and imaginary refractive indices can be used as perfect absorbers [10]. Such materials have been realized with layered cermets (ceramic matrix/metal composites) [11],[12]. A perfectly matched layer (PML) used in finite difference time domain simulations is also, in principle, a perfect absorber. However, a PML is not physically realizable for solar radiation as it requires a non-zero imaginary part of magnetic permeability [13]. A SEH with a high φ also ultimately requires a large absorption coefficient $\alpha \equiv 4\pi k / \lambda$ to maximize absorption for a given mass. Here, k is the imaginary part of the refractive index or the extinction coefficient and λ is the wavelength of light in vacuum. Dreissen et al. have discussed this for NbN thin-films [14].

Homogenous single phase materials have a unique refractive index for a given wavelength. In order to create a gradient, it is necessary to vary the refractive index in a smooth manner. Heterogeneous materials can be tailored to have effective intermediate optical properties for this purpose. In this work noble metal nanoparticle/dielectric matrix optical composites are considered. The nanoparticles are considered spherical for simplicity in the analysis. Noble metal NPs are chosen because the optical properties of their composites are influenced by the localized surface plasmon resonance (LSPR). LSPR is known to occur in the solar spectrum for noble metals like Ag, Au and Cu [2]. LSPR leads to a large value of absorption cross-section in these NPs and hence a large value of absorption coefficient of the optical composite. The resonant response depends on the material, size and structure of the NP allowing tunability [2],[3]. Hence, in principle, the control of inclusions' concentrations along with the above mentioned tunable parameters can allow for the design of optical composites with desired spectral optical constants (see for example Ref. [5]).

If the practical difficulties in fabrication are neglected then, the problem of rational design criteria for such metal NP/dielectric matrix composites still stands. With this in mind, an attempt at solving the following set of problems forms the main part of this work.

1. Prediction of optical properties of non-graded single and two metal NP/dielectric composites through the finite difference time domain (FDTD) simulation method with focus on variation with the following parameters:

   - NP diameter d

   - Volume fractions f

   - Ratio of the individual NP species volume fractions in case of ternary composites.

2. Comparison of the predicted properties with some widely used effective medium theories (EMTs) and their extensions.

3. Demonstration of plasmonics-based solar energy harvesting for a real system; namely wavelength specific control of light intensity for phototrophic growth of microalgae.

Chapter 2

Theory and Computational Methods

2.1　Introduction

Spatially inhomogeneous, complex or composite media assume physical properties that are different from their component materials. In itself a "small sample" exhibits spatially inhomogeneous physical properties but a "bulk sample" exhibits a homogeneous set of physical properties. This occurs as a result of spatial averaging of associated fields in the bulk. The definition of bulk depends on the length scale of the inhomogeneities. In case of optical composites, the physical properties under consideration are the relative electric permittivity ε_r and the magnetic permeability μ_r. The associated fields are the electric $\mathbf{E}$ and magnetic $\mathbf{H}$ fields. The homogenized or effective physical properties are taken to be ε_{eff} and μ_{eff} (the subscript 'r' representing relative is dropped from now on for simplicity). The governing equations are the Maxwell's equations in the following form.

$$\nabla \cdot \left(\varepsilon_0 \varepsilon_r \mathbf{E} \right) = 0 \tag{2.1a}$$

$$\nabla \cdot \mathbf{H} = 0 \tag{2.1b}$$

$$\nabla \times \mathbf{E} = -\mu_0 \mu_r \frac{\partial \mathbf{H}}{\partial t} \tag{2.1c}$$

$$\nabla \times \mathbf{H} = \varepsilon_0 \varepsilon_r \frac{\partial \mathbf{E}}{\partial t} + \sigma \mathbf{E} \qquad (2.1\text{d})$$

All variables in eqs 2.1 take real values. Here σ is the conductivity of the medium and; ε_0 and μ_0 are the permittivity and the permeability of the vacuum. The magnetic response of materials in the UV-Visible-IR (Solar) frequency region is negligible and hence $\mu = 1$ in eqs. 2.1. Hence only ε_{eff} was the effective property under consideration here. It is assumed that there was no free charge or current present in the medium under consideration. The following are the boundary conditions that are applicable to an interface separating two materials with different relative permittivities.

$$(\varepsilon_1 \mathbf{E}_1) \cdot \hat{\mathbf{n}} = (\varepsilon_2 \mathbf{E}_2) \cdot \hat{\mathbf{n}} \qquad (2.2\text{a})$$

$$\mathbf{E}_1 \times \hat{\mathbf{n}} = \mathbf{E}_2 \times \hat{\mathbf{n}} \qquad (2.2\text{b})$$

$$\mathbf{H}_1 = \mathbf{H}_2 \qquad (2.2\text{c})$$

Here $\hat{\mathbf{n}}$ is a unit vector normal to the interface. The interface under consideration is between materials with relative permittivities ε_1 and ε_2. Notice that the subscript 'r,' representing relative has been dropped for the sake of simplicity. Eq. 2.2a means that the normal component of the electric displacement $(\varepsilon \mathbf{E})$ is continuous across the interface. Eq. 2.2b

9

implies that the tangential component of $\mathbf{E}$ is continuous across the interface. Magnetic field $\mathbf{H}$ is continuous across the interface according to eq. 2.2c.

The time-dependent Maxwell equations (eqs. 2.1) can be simplified to a time-independent vector Helmholtz equation (VHE) for an electric field with a complex time-independent amplitude $\tilde{\mathbf{E}}(\mathbf{r})$. This is done by substituting a plane wave like solution of the form $\tilde{\mathbf{E}}_0 e^{i(\tilde{\mathbf{k}}\cdot\mathbf{r}-\omega t)} = \tilde{\mathbf{E}}(\mathbf{r})e^{-i\omega t}$ into eqs. 2.1. Here $\tilde{\mathbf{E}}_0$ is the complex amplitude of the wave, $\tilde{\mathbf{k}}$ is it's complex wave vector and ω is it's angular frequency [3]. Eq. 2.3a is the obtained VHE and eq. 2.3b gives the form of $\tilde{\mathbf{k}}$.

$$(\nabla^2 + \tilde{\mathbf{k}}\cdot\tilde{\mathbf{k}})\tilde{\mathbf{E}} = 0 \tag{2.3a}$$

$$\tilde{\mathbf{k}} = \frac{2\pi\omega}{c}\tilde{\varepsilon}(\omega)\hat{\mathbf{p}} \tag{2.3b}$$

In eq. 2.3b, $\hat{\mathbf{p}}$ is a unit vector in the direction of propagation and $\tilde{\varepsilon}(\omega)$ is the complex permittivity of the medium. Complex values are used to simplify the analysis. By doing so, it is possible to incorporate the loss due to electron transport in the imaginary part of the wave vector and permittivity. Complex value of the field amplitude $\tilde{\mathbf{E}}_0 = \mathbf{E}_0 e^{i\theta}$ incorporates the phase information through θ.

In the electrostatic case ($\tilde{\mathbf{k}} \to \mathbf{0}$), the VHE can be further simplified to a Laplace equation. In this case, eq. 2.1a fully describes the electric field $\mathbf{E}$. If $\mathbf{E} = -\nabla\phi$, where ϕ is a potential; and the medium under consideration is homogenous, then eq. 2.1a transforms to the Laplace equation as in eq. 2.4.

$$\nabla^2 \phi = 0 \tag{2.4}$$

Continuity of the potential ϕ across an interface supplements the boundary conditions represented by eqs. 2.2. Eqs. 2.1-4 completely describe the behavior of electric and magnetic fields inside a homogenous material for various conditions described above. The boundary conditions represented by eqs. 2.2 are applicable without loss of generality to eqs. 2.3a and 2.4.

2.2   Effective Medium Theories

Effective linear dielectric response ε_{eff} of a composite material is a function of the following variables: permittivity of the matrix ε_m; permittivities of the n species of inclusion particles ε_{pi} (i=1, 2, 3 … n); volume fractions f_i of each inclusion species; and size, shape and spatial distributions of each inclusion species. Fig. 2.2 is a schematic of a finite region of an infinite 2-D binary composite with spherical inclusions of permittivity ε_p embedded in a matrix of permittivity ε_m. Presence of inhomogeneities leads to local perturbations in $\mathbf{E}$ and $\mathbf{H}$. The effective permittivity ε_{eff} corresponds to the spatially averaged fields $\mathbf{E}_{\mathbf{avg}}$ and $\mathbf{H}_{\mathbf{avg}}$.
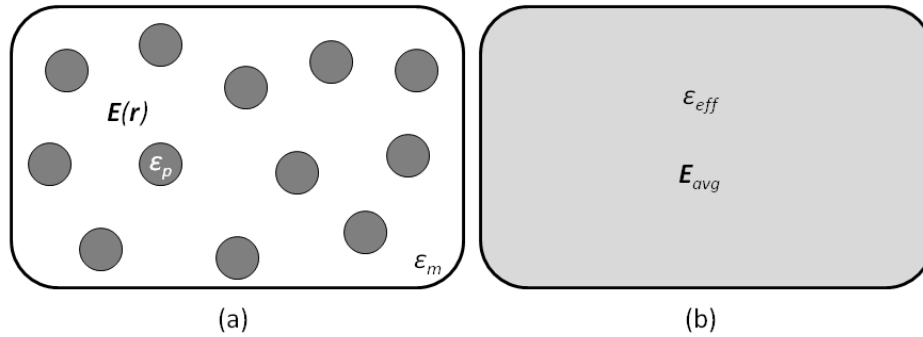
Figure 2.2: (a) A schematic of the microstructure of a 2-D composite with one type of inclusion embedded in an infinite matrix with a perturbed electric field, (b) homogenized composite with uniform average electric field and permittivity.

For the purpose of this work it is assumed that the inclusions are monodisperse spheres randomly distributed in the matrix. They do not touch each other. Further, it is assumed that the effective properties correspond to an infinite 3-D composite at a steady-state with respect to the applied field; and the effective properties could be estimated by averaging over a volume that was large enough compared to the spatial scale of the inhomogeneties.

Traditionally, the methods of estimating the effective properties are called effective medium theories (EMTs), effective medium approximations (EMAs) or mixing rules. Various EMTs have been proposed [15]. The first one was proposed in 1905 by J. C. Maxwell-Garnett [16]. Each EMT is based on a set of simplifying assumptions. Here, some widely used EMTs for spherical inclusions based composites will be discussed. Simplest EMTs are for binary composites i. e., composites with only one type of inclusions in a homogenous lossless dielectric matrix. Further, it is assumed that the inclusions are spherical, vanishingly small compared to the applied wavelength of light, spatially random, and have a very low volume

fraction. The Maxwell-Garnett EMT (MGEMT) is based on the solution of the Laplace equation (eq. 2.4) [15] and gives the following result.

$$\varepsilon_{eff}(p, f, m) = \varepsilon_m \frac{\varepsilon_p(1 + 2f) - \varepsilon_m(2f - 2)}{\varepsilon_p(1 - f) + \varepsilon_m(2 + f)}. \tag{2.5}$$

Here f is the volume fraction of the inclusions in the composite. Note that the denominator in eq. 2.5 represents the plasmon resonance condition for $f \to 0$ i. e., $\varepsilon_p = -2\varepsilon_m$. As f increases, there is a red-shift in the resonance wavelength. Further, eq. 2.5 only accounts for the presence of one type of inclusion. Garcia et al. have proposed an extension wherein multiple species of inclusions (p_i) can be accounted for by first calculating $\varepsilon_{eff}(p_i, f_i, m)$ followed by application of the MGEMT to these effective permittivities in a hierarchical manner [6].

2.3   The Finite Difference Time Domain (FDTD) Method

The FDTD method was used to simulate the linear dielectric behavior of binary and ternary plasmonic composite materials subject to solar frequency range (UV-Vis-NIR) radiation. Commercial software OptiFDTD was adapted for the simulations. The FDTD method is a direct march-in-time simulation of the Maxwell's curl equations (eqs. 2.1) over a decretized spatial domain. The Yee cell, shown in fig. 2.3, is used as the 3-D spatial unit cell. The Maxwell's equations are decretized in the following manner [13].

$$H_x\Big|_{i,j-1/2,k-1/2}^{n+1/2} = H_x\Big|_{i,j-1/2,k-1/2}^{n-1/2} + \frac{\Delta t}{\mu_0 \Delta z}\left(E_y\Big|_{i,j-1/2,k}^{n} - E_y\Big|_{i,j-1/2,k-1}^{n}\right)$$

$$-\frac{\Delta t}{\mu_0 \Delta y}\left(E_z\Big|_{i,j,k-1/2}^{n} - E_z\Big|_{i,j-1,k-1/2}^{n}\right) \tag{2.6a}$$

$$H_y\Big|_{i-1/2,j,k-1/2}^{n+1/2} = H_y\Big|_{i-1/2,j,k-1/2}^{n-1/2} + \frac{\Delta t}{\mu_0 \Delta x}\left(E_z\Big|_{i,j,k-1/2}^{n} - E_z\Big|_{i-1,j,k-1/2}^{n}\right)$$

$$-\frac{\Delta t}{\mu_0 \Delta z}\left(E_x\Big|_{i-1/2,j,k}^{n} - E_x\Big|_{i-1/2,j,k-1}^{n}\right) \tag{2.6b}$$

$$H_z\Big|_{i-1/2,j-1/2,k}^{n+1/2} = H_z\Big|_{i-1/2,j-1/2,k}^{n-1/2} + \frac{\Delta t}{\mu_0 \Delta y}\left(E_x\Big|_{i-1/2,j,k}^{n} - E_x\Big|_{i-1/2,j-1,k}^{n}\right)$$

$$-\frac{\Delta t}{\mu_0 \Delta x}\left(E_y\Big|_{i,j-1/2,k}^{n} - E_y\Big|_{i-1,j-1/2,k}^{n}\right) \tag{2.6c}$$

$$E_x\Big|_{i-1/2,j,k}^{n+1} = \left(\frac{2\varepsilon - \sigma\Delta t}{2\varepsilon + \sigma\Delta t}\right)E_x\Big|_{i-1/2,j,k}^{n}$$

$$+\frac{1}{\Delta y}\left(\frac{2\Delta t}{2\varepsilon + \sigma\Delta t}\right)\left(H_z\Big|_{i-1/2,j+1/2,k}^{n+1/2} - H_z\Big|_{i-1/2,j-1/2,k}^{n+1/2}\right)$$

$$-\frac{1}{\Delta z}\left(\frac{2\Delta t}{2\varepsilon + \sigma\Delta t}\right)\left(H_y\Big|_{i-1/2,j,k+1/2}^{n+1/2} - H_y\Big|_{i-1/2,j,k-1/2}^{n+1/2}\right) \tag{2.6d}$$

$$E_y\Big|_{i,j-1/2,k}^{n+1} = \left(\frac{2\varepsilon - \sigma\Delta t}{2\varepsilon + \sigma\Delta t}\right)E_y\Big|_{i,j-1/2,k}^{n}$$

$$+\frac{1}{\Delta z}\left(\frac{2\Delta t}{2\varepsilon + \sigma\Delta t}\right)\left(H_x\Big|_{i,j-1/2,k+1/2}^{n+1/2} - H_x\Big|_{i,j-1/2,k-1/2}^{n+1/2}\right)$$

$$-\frac{1}{\Delta x}\left(\frac{2\Delta t}{2\varepsilon + \sigma\Delta t}\right)\left(H_z\Big|_{i+1/2,j-1/2,k}^{n+1/2} - H_z\Big|_{i-1/2,j-1/2,k}^{n+1/2}\right) \tag{2.6e}$$

$$E_z\Big|_{i,j,k-1/2}^{n+1} = \left(\frac{2\varepsilon - \sigma\Delta t}{2\varepsilon + \sigma\Delta t}\right)E_z\Big|_{i,j,k-1/2}^{n}$$

$$+ \frac{1}{\Delta x}\left(\frac{2\Delta t}{2\varepsilon + \sigma\Delta t}\right)\left(H_y\Big|_{i+1/2,j,k-1/2}^{n+1/2} - H_y\Big|_{i-1/2,j,k-1/2}^{n+1/2}\right) \tag{2.6f}$$

$$- \frac{1}{\Delta y}\left(\frac{2\Delta t}{2\varepsilon + \sigma\Delta t}\right)\left(H_x\Big|_{i,j+1/2,k-1/2}^{n+1/2} - H_x\Big|_{i,j-1/2,k-1/2}^{n+1/2}\right)$$
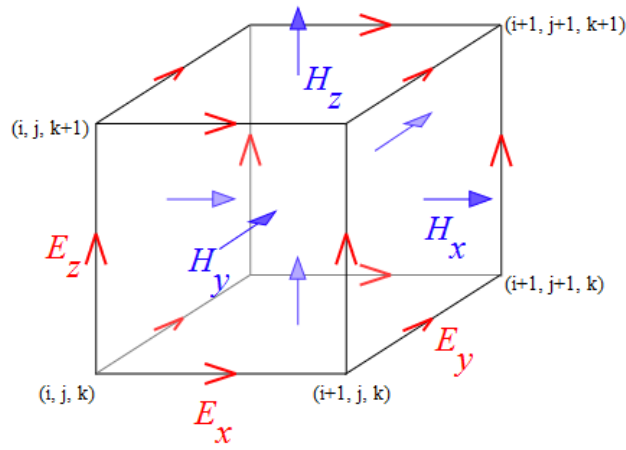
Figure 2.3: A schematic of the Yee cell. Notice that the E and H field components are located at edge and face centers of the cuboid grid in order to facilitate the decretization of Maxwell's curl equations.

Superscript n denotes the time iteration number and subscripts i, j, and k represent the discretized spatial coordinates of the electric field $(E_x(t), E_y(t), E_z(t))$ and the magnetic field $(H_x(t), H_y(t), H_z(t))$. Field components (E_x, E_y, E_z) and (H_x, H_y, H_z) are not located at the vertices (i,j,k) but instead at the edge and face centers of the cuboidal lattice.

Hence they assume coordinates like $(i-\frac{1}{2}, j, k)$, $(i+\frac{1}{2}, j+\frac{1}{2}, k)$ etc. The electric field components (E_x, E_y, E_z) lie on the edge centers and the magnetic field components (H_x, H_y, H_z) lie on the face centers in fig 2.3. The assignment of edge and face center

15

positions to the field components is arbitrary in the sense that their positions can be interchanged without altering the computational scheme. The main reason for such a position assignment is the facilitation of iterative calculation of the curl of each field at each time step as is required by the Maxwell's equations. The numerical scheme is second order accurate as it considers central differences in space and time. The scheme is explicit in nature and requires the following (Courant-Friedrichs-Lewy) stability condition be satisfied [13]:

$$\Delta t \le \frac{1}{\dfrac{c}{n}\sqrt{\dfrac{1}{(\Delta x)^2} + \dfrac{1}{(\Delta y)^2} + \dfrac{1}{(\Delta z)^2}}} \qquad (2.7)$$

Here Δt is the time step; and Δx, Δy and Δz represent the Cartesian mesh in 3-dimensions. The refractive index of the medium under consideration is given by n and c is the speed of light in vacuum. The time step and the mesh are kept constant throughout the simulation. The mesh size is chosen in such a way that

Special boundary conditions know as "perfectly matched layers" (PML) are used for FDTD simulations as artificial reflectionless perfectly absorbing layers to truncate an infinite simulation domain. For the purposes of the current work, asymmetric or uniaxial PML (APML) boundary conditions were used to truncate the domain in ±Z directions. APML works by choosing ε and μ for the absorbing boundary layer subject to the condition that the Fresnel reflection coefficient is zero for all angles of incidence. The parameters $\bar{\varepsilon}$ and $\bar{\mu}$ for the APML that is perpendicular to the Z direction and adjacent to a material with an isotropic permittivity ε_i^0 are given by the following relationships [13]:

16

$$\frac{\overline{\varepsilon}}{\varepsilon^i} = \overline{\mu} = \overline{s} = \begin{bmatrix} 1 + \dfrac{\sigma(z)}{i\varepsilon_0\omega} & 0 & 0 \\[4mm] 0 & 1 + \dfrac{\sigma(z)}{i\varepsilon_0\omega} & 0 \\[6mm] 0 & 0 & \dfrac{1}{1 + \dfrac{\sigma(z)}{i\varepsilon_0\omega}} \end{bmatrix}, \qquad (2.8a)$$

$$\text{where, } \sigma(z) = \frac{\sigma_{max}|z - z_0|^m}{d^m}. \qquad (2.8b)$$

Here, the boundary is located at $z = z_0$; d is the thickness of the APML layer, $m>1$ is the power of the polynomial that describes the increasing conductivity $\sigma(z)$ and σ_{max} is a pre-multiplier. Conductivity $\sigma(z)$ is made to vary with z to make the transition into the APML smooth for minimal Fresnel reflection. Note that from the form of eqs. 2.8a, it is necessary for ε_i^0 to be real, i. e., an APML boundary cannot be placed adjacent to a lossy material. In the present study, the theoretical reflection coefficient (disregarding spatial descretization of the APML) was set at 0.3%.

The software was benchmarked by comparing theoretical and simulated reflectances R^{th} and R^{sim} respectively for a $t = 300\text{nm}$ thick SiO_2 slab with refractive index n_{SiO_2} for the wavelength range $\lambda = 300$ to 800nm. R^{th} was calculated with the following equations.

17

$$r = \frac{1 - n_{SiO_2}}{1 + n_{SiO_2}} \qquad (2.9a)$$

$$b = \exp\left(\frac{i4\pi n_{SiO_2} t}{\lambda}\right) \qquad (2.9b)$$

$$R^{th} = \left|\frac{r(1-b)}{1 - r^2 b}\right|^2 \qquad (2.9c)$$

Fig. 2.4 shows a comparison of the theoretical and simulated values of R. The values are seen to be in good agreement with one another. The difference was attributed to that fact that experimentally obtained values of n_{SiO_2} were used for computing R^{th} while a Lorentz-Drude fit to the experimental values was used to obtain R^{sim} [13],[17].
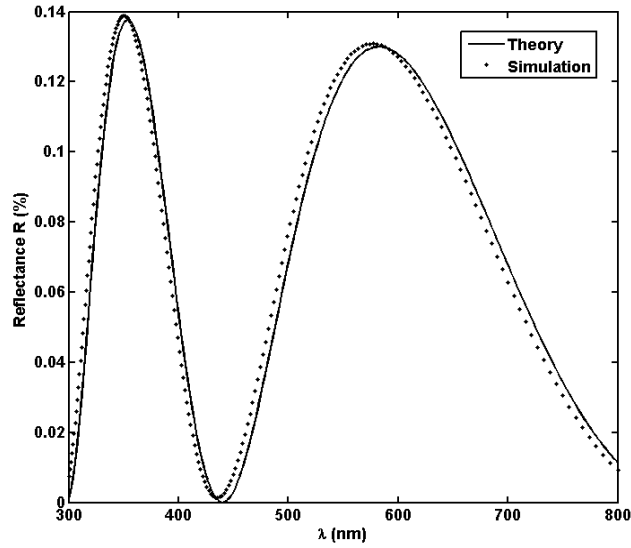
Figure 2.4: A comparison of theoretical and simulated reflectances (R^{th} and R^{sim}) from a 300 nm thick SiO$_2$ slab over the wavelength range of interest.

18

Fig 2.5 shows the 2-D projection of the 3-D domain used in the simulations. The following conditions were used for all simulations.

- A 10d X 10d X 10d box was used to represent the composite with spherical inclusions with diameters d. The simulation domain was a 10d X 10d X 12d box with a 1d spacing before and after the composite in the Z direction.

- The spherical inclusions were assigned spatially random locations in the box. However, their locations were assigned is such a way that each particle did not touch any other particles. Further, the particles were constrained to be fully inside the box so that they maintained their spherical identity.

- A normally incident Y-polarized Gaussian modulated rectangular wave travelling in the $+Z$ direction with a carrier wavelength of 400 nm was chosen to be the input field. The half width was set to obtain data in the 300 to 800nm wavelength range. This facilitated extraction of spectral information from a single simulation. The input plane was set at $z = 0.2d$.

- It was assumed that a thin slab of thickness $10d$ was a good representation of the composite. Hence, APML boundary conditions were used for $\pm Z$ boundaries and periodic boundary conditions were used for $\pm X$ and $\pm Y$ boundaries.

- Observation areas for measuring the reflectance R and transmittance T were set so they were one mesh point outside the composite. This was done so that radiant power in all directions could be accounted for.

The effective permittivity $\varepsilon_{\textit{eff}}$ was extracted from the measured R and T values by simultaneously inverting eq. 2.9c for theoretical reflectance R^{th} along with the following equation for the theoretical transmittance T^{th}:

$$T^{th} = \left| \frac{(1-r^2)\sqrt{b}}{1-r^2 b} \right|^2 . \tag{2.9d}$$
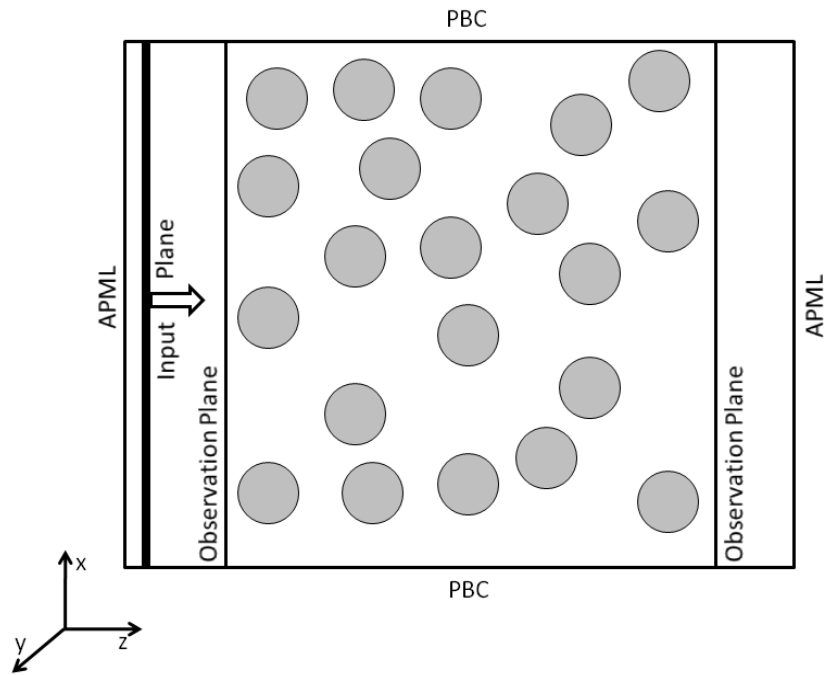
Figure 2.5: A schematic of the simulation domain used for the FDTD simulations.

Chapter 3

Binary and Ternary Composites

3.1 Binary Composites

The Maxwell-Garnett effective medium theory (MGEMT) is applicable to both dielectric/dielectric and metal/dielectric (plasmonic composites) binary composites. In order to verify the applicability of the FDTD simulation approach, it was first tested against the MGEMT for a dielectric/dielectric composite with varying volume fractions. The simulation conditions were as mentioned in the previous chapter, except that the simulations were performed for a continuous wave input field with $\lambda = 3000$ nm. The inclusion particles were assigned a permittivity of $\varepsilon_p = 9$ while the permittivity of the matrix was set to $\varepsilon_m = 1$. The

particle diameter was set to 20 nm so that the parameter $x = \dfrac{\pi d \sqrt{\varepsilon_m}}{\lambda} \ll 1$. This condition is

necessary for the MGEMT to be applicable [3]. Simulations were performed for random as well as cubic ordered composites. Fig. 3.1 shows the extracted effective permittivities for both the cases. A good agreement was found between MGEMT and simulations for small values of volume fraction f. In case of a cubic arrangement, the theory over-predicted the effective permittivity while in case of random arrangement, there was an under-prediction. The deviation increased with f. This was attributed to an increase in the inter-particle field interactions as they were packed closer to each other. Further, the slight deviation that does exist, even at small values of f, is due to the fact that x is finite.
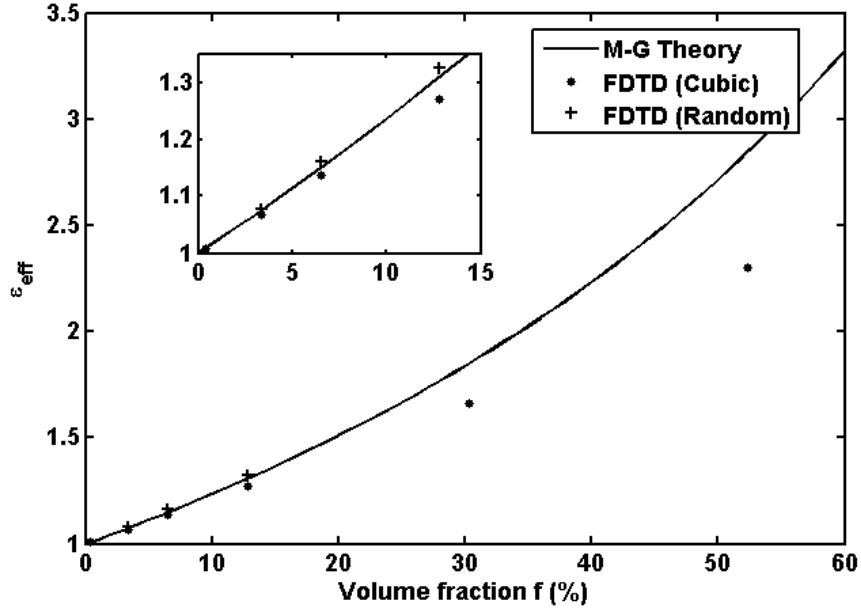
Figure 3.1: Comparison of MGEMT with extracted effective permittivities for random and ordered dielectric/dielectric composites with various inclusion volume fractions.(*d*=20nm and *λ*=3000nm)

Fig. 3.2 shows a comparison of the simulated absorptance A of Ag/air binary plasmonic composites slabs in air with $f = 0.02$, $d = 1$, 10 and 100nm and thickness $t = 10d$ with the corresponding MGEMT values of $\lambda = 300$ to 800nm. The mesh size was set to $\Delta x = \Delta y = \Delta z = 0.1d$. A deviation was observed in the plasmonic peak position and the overall shape of the response even for small values of d (1 and 10nm). This was attributed to the coarseness of the mesh. As fig. 3.3 shows, for $d = 10$nm, there was an improvement in the response in comparison to the MGEMT when the mesh was refined to $\Delta x = \Delta y = \Delta z = 0.05d$ and $0.0334d$. Large deviations from the theoretical value occur for $\lambda > 400$ nm. This is attributed to the fact that the small penetration depth at those wavelengths (fig. 3.3, inset) leads to an enhanced sensitivity to the mesh size. Further, as fig. 3.4 shows, the contribution to the error in A due to consideration of only one realization

22

was negligible. In it, the error in A over five realizations for $f = 0.02$ and $d = 10$nm was

~2%.
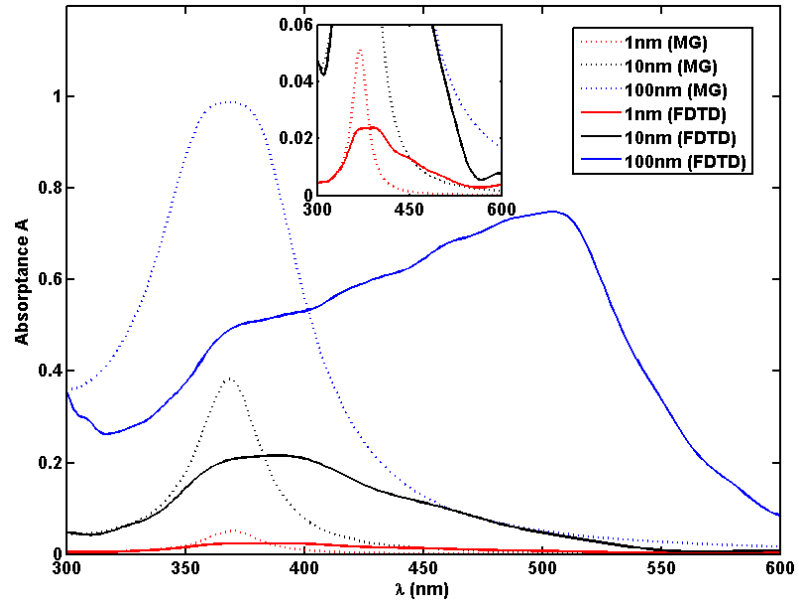
Figure 3.2: Comparison of MGEMT and simulated absorptances *A* for Ag/Air plasmonic composites with various *d*. Mesh size was 0.1*d*.
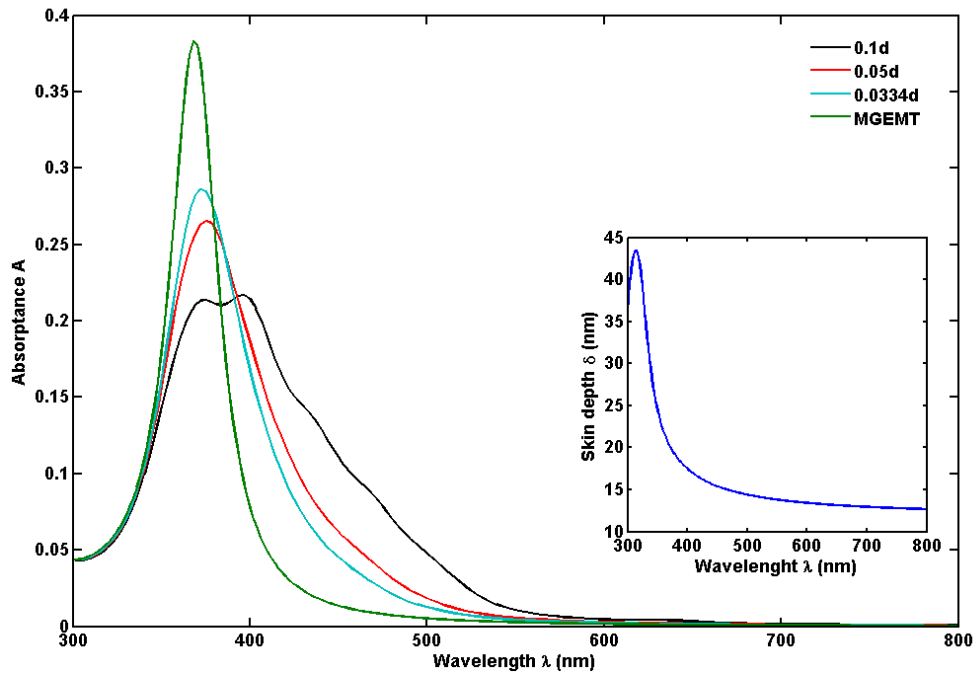
Figure 3.3: Effect of mesh refinement on the response of *d*=10nm Ag/Air plasmonic composite compared to MGEMT. The inset shows the variation of optical skin depth of Ag with the wavelength.
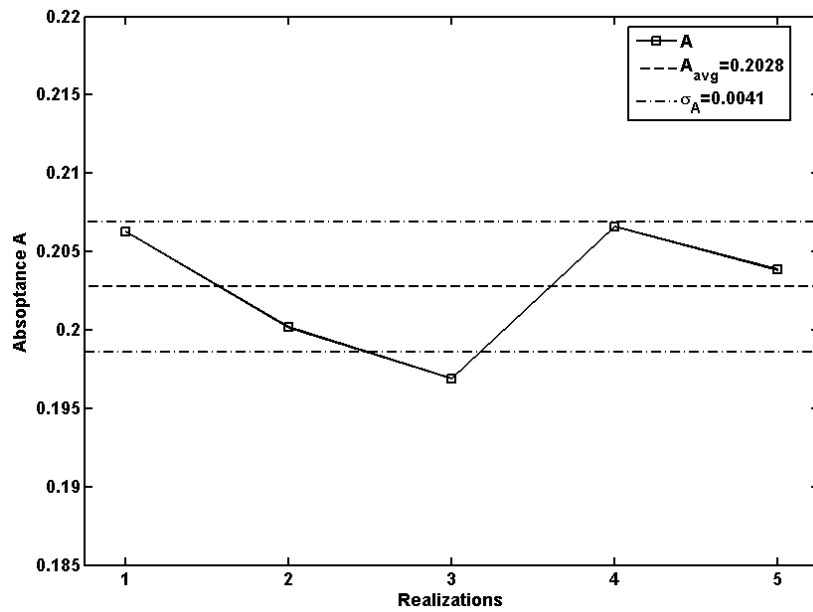
Figure 3.4: Variation in *A* for five realization for Ag/Air plasmonic composite with *f*=0.02.

3.2   Ternary Composites

Ag/Cu/SiO$_2$ ternary plasmonic composites were considered for this part of the work. Magruder et al. [18] have fabricated such composites with various Ag:Cu ratios. They have done this by sequentially implanting Ag and Cu ions in to SiO$_2$ substrates. The substrates (Corning 7940) had a thickness larger than one millimeter. The concentration profiles were measured with the Rutherford backscattering (RBS) technique. The maxima in the concentrations of Ag and Cu were reported to be ~140nm and ~130nm respectively. This ensured that both the species were approximately present at similar depths in the sample. Further, the samples were fabricated at 270K and not annealed after that. This ensured presence of Ag and Cu as separate species and hence formation of a ternary composite. The average particle diameter was reported to be 30nm [18]. Hence, simulations were performed for a composite slab with inclusion diameters $d = 30$nm. The process of ion implantation leads to the formation of a spatially non-uniform ion concentration profile through the depth of the sample. The implanted ions form particles by the process of diffusion. Hence a particle size distribution along with a depth profile of the particle volume fraction is expected from this fabrication technique. The actual ternary composite existed only near one surface of the sample. The total volume fraction f of the inclusions was assigned an arbitrary value of 0.02 for the purpose of the FDTD simulations.

The optical properties were reported as the optical density (OD). OD is defined in the following manner:

$$OD \equiv -\log_{10} \frac{T_{sample}}{T_{SiO_2}} \tag{3.1a}$$

$$\text{where, } T = I_0 - I . \tag{3.1b}$$

Here T is the transmittance, $I_0(\lambda)$ is the probe intensity and $I(\lambda)$ is the measured intensity. Fabry-Perot like oscillations in the spectrum caused by multiple internal reflections can be neglected as the sample under consideration is orders of magnitude thicker than the optical wavelengths. This means that a sample without implantation would always have had $T_{SiO_2} \sim 1$. Thus, $A_{sample} \sim 1 - 10^{-OD}$.

Fig. 3.5 shows a comparison of simulated and experimental values of absorptance A for Ag:Cu ratios 1:1 and 1:3. The extracted absorbance values from the experimental data were scaled by an arbitrary multiplying factor to accommodate for the uncertainty in thickness and volume fraction. A fair agreement was found, although the peaks associated with Ag and Cu appeared at marginally different wavelengths. This was attributed to the fact that there existed a particle size distribution and a spatial profile in the experimental samples as discussed previously. Size distribution gives rise to peak broadening and shifting while spatial profile leads to a spatial variation in the volume fraction and hence the optical properties.

Fig 3.6 shows a comparison of absorptance A calculated with Garcia et al.'s extended EMT for ternary composites [6] and FDTD simulations for $Ag/Cu/SiO_2$ ternary plasmonic composites mentioned previously. Simulated peak for Cu was blue-shifted and was red-shifted for Ag. Disagreement was attributed to two main factors: (1) coarseness of mesh and (2) the fact that FDTD simulation requires a Lorentz-Drude fit of experimental permittivity data.

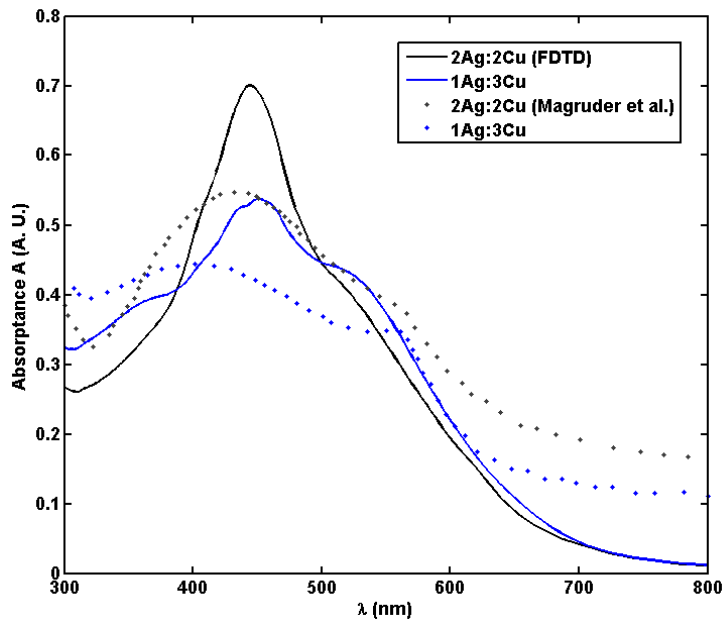**Figure 3.5: Comparison of simulated and experimental [18] optical response of Ag/Cu/SiO₂ plasmonic composites for two Ag:Cu ratios. The experimental data was rescaled to accommodate experimental uncertainty. Mesh size for the FDTD simulations was 0.05*d*.**
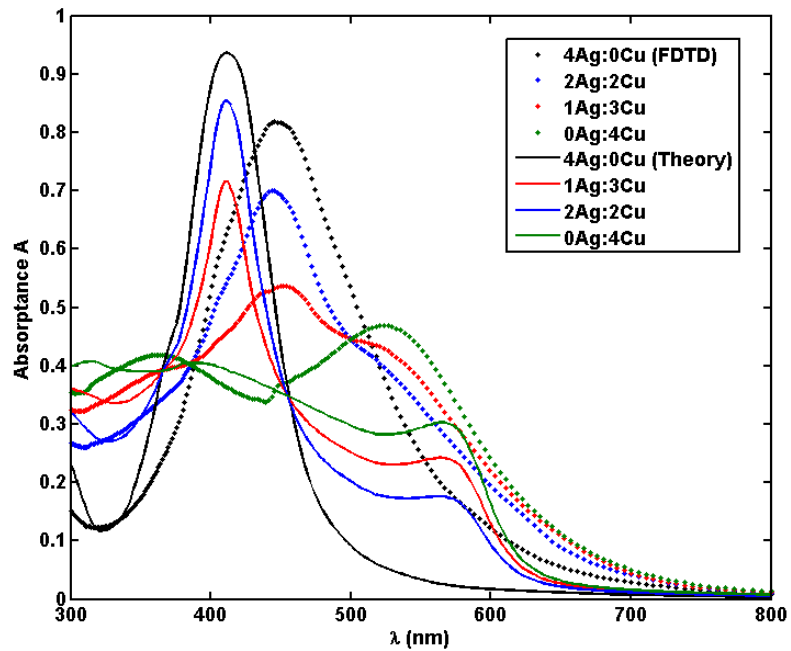
Figure 3.6: Comparison of FDTD simulation and Garcia et al.'s EMT [6] based calculations of the optical response of Ag/Cu/SiO₂ plasmonic composites. Mesh size was 0.05*d*.

Chapter 4

Plasmon-Enhanced Microalgal Growth in Mini-Photobioreactors

(*Contents taken from:* S. Torkamani, S. N. Wani, Y. J. Tang and R. Sureshkumar, "Plasmon-enhanced microalgal growth in miniphotobioreactors," *Appl. Phys. Lett.*, vol. 97, 2010, p. 043703)

4.1 Introduction

In this chapter, the application of wavelength specific reflective nature of plasmonic composites to enhancement of photosynthetic microalgal growth is discussed. Here, the composite is in the form of a suspension. As discussed earlier, the ability to tune the plasmon resonance frequency by varying the size, shape, architecture and/or concentration of the NPs offers a means to tailor materials to a desired application requiring wavelength specificity [2].

The metabolic activity of several photoactive microalgae is not uniform throughout the electromagnetic (EM) spectrum, e.g., green microalga (MA) *Chlamydomonas reinhardtii*, exhibits two peaks, in the blue and red regions of the EM spectrum [19]. (A comparison of the spectral range of photoactivity of *Chlamydomonas reinhardtii* with the calculated plasmon resonance frequency of spherical Ag NP suspensions used in this work can be found in Fig. 4.1.) This is because algal photoactive pigments work only in specific ranges of the spectrum [20], while certain other wavelengths (e.g. 520-680 nm) may cause photoinhibition [21],[22]. Hence, it is advantageous to enhance light only in the wavelength range favorable to the

growth of the organism. Further, light selectivity in bioreactors would reduce the growth of

contaminant photosynthetic microorganisms that are photoactive in the wavelength range in

which the desired species is not photoactive.
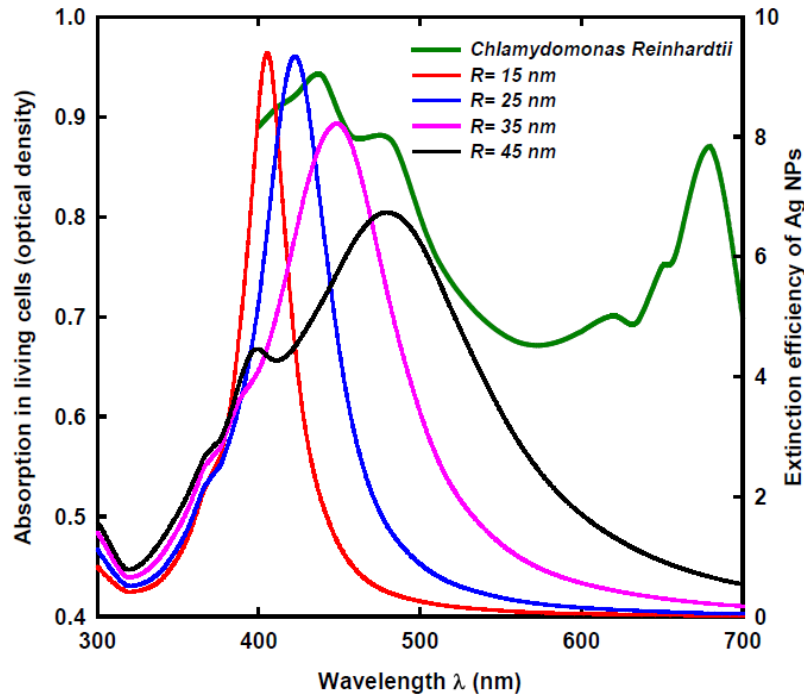
Figure 4.1: Plasmonic response spectra of spherical Ag NPs of various radii *R* suspended in water compared to the absorption spectrum of microalga *Chlamydomonas reinhardtii*. Notice the red-shift and loss in the sharpness of the peak for increasing NP radius. *R* ~ 25 nm gives highest peak

Algal growth requires both sufficient light intensity and optimal wavelength. Various

methods have been proposed to reduce the light intensity attenuation in the cell culture

[23],[24]. However, to date, wavelength specificity of backscattering of light has not been

utilized as means for promoting phototrophic algal growth. The present approach takes

advantage of LSPR of metal nanoparticles (NPs). Resonant interactions of light (photons)

and surface plasmons can be used to amplify light absorption/scattering at specific

wavelengths. This idea was verified for a miniature microalgal photobioreactor (PBR). In a broad sense, the NP suspension functions as a mirror but with important advantages. First, the scattered total light flux to the microalgae culture can be precisely controlled by changing the NP concentration and size [2]. Hence photoinhibition can be avoided. Second, the frequency of the scattered light can be tuned by varying the shape and size of the NPs. For example, spherical Ag NPs scatter light in the blue region of the EM spectrum [3] which can be utilized for MA growth. Third, the fluid nature of NP suspensions allows shape flexible and efficient backscattering in PBRs. Such plasmonic mini-PBRs (PMPBRs) have potential applications in MA-based biosensors to detect toxic compounds [25-27] in the natural environment, especially under limited ambient light.

4.2   Mathematical Model

The PMPBR configuration used in the present study is schematically illustrated in Figure 4.2a. It consists of two separate compartments: one containing the MA culture and the other containing the NP suspension. Light is incident perpendicular to the top surface of the MA compartment. For this system, a mathematical model is developed to test the feasibility of the approach and offer guidelines to the experiments. This model describes the irradiance and the resulting microalgal growth for *Chlamydomonas reinhardtii* as function of NP (Ag) concentration and size. Let the autotrophic specific MA growth rate be denoted by μ_p (s^{-1}). Then growth rate $r_X \equiv \mu_p X$ where X is the biomass concentration (kg m^{-3}). Light dependency of photosynthetic growth is modeled as:[19]

$$\mu_p = \mu_{max} \frac{F}{K_I + F + \dfrac{F^2}{K_{II}}}. \qquad (4.1)$$

In eq. 4.1, K_I is the half saturation constant (mol photon m^{-2} S^{-1}), K_{II} is the inhibition constant (mol photon m^{-2} S^{-1}) and F is the irradiance (mol photon m^{-2} S^{-1}) which is a function of space and time. The two flux model is used for F which is assumed to vary only along the depth (z) of the culture [28]:

$$\pm \frac{1}{X} \frac{dF^{\pm}}{dz} = E_a F^{\pm} + bE_S F^{\pm} - bE_S F^{\mp}. \qquad (4.2)$$

In eq. 4.2, E_a and E_S represent the mass absorption and scattering coefficients (m^2 kg^{-1}), b represents the backscattering coefficient of the MA/NP and the superscripts +/- denote forward/backward travelling fluxes respectively. The parameters related to phototrophic MA growth in eqs. 4.1 and 4.2 are obtained from the literature [29],[28]. The values of E_a and E_S for the NPs are calculated by utilizing Mie theory assuming spherical NPs in a dilute monodisperse suspension with $b = 0.5$ [3]. Eqs. 4.1 and 4.2 are solved numerically for the entire PMPBR with appropriate (continuity) boundary conditions to calculate the available irradiance $F(z,t)=F^+(z,t)+F^-(z,t)$. The enhancement in the biomass concentration, x, is defined as $x \equiv (X_{NP} - X)/X$, where the subscript NP signifies growth conditions in presence of backscattering from the NP suspension while X corresponds to the control experiments which entailed algal growth without backscattering.
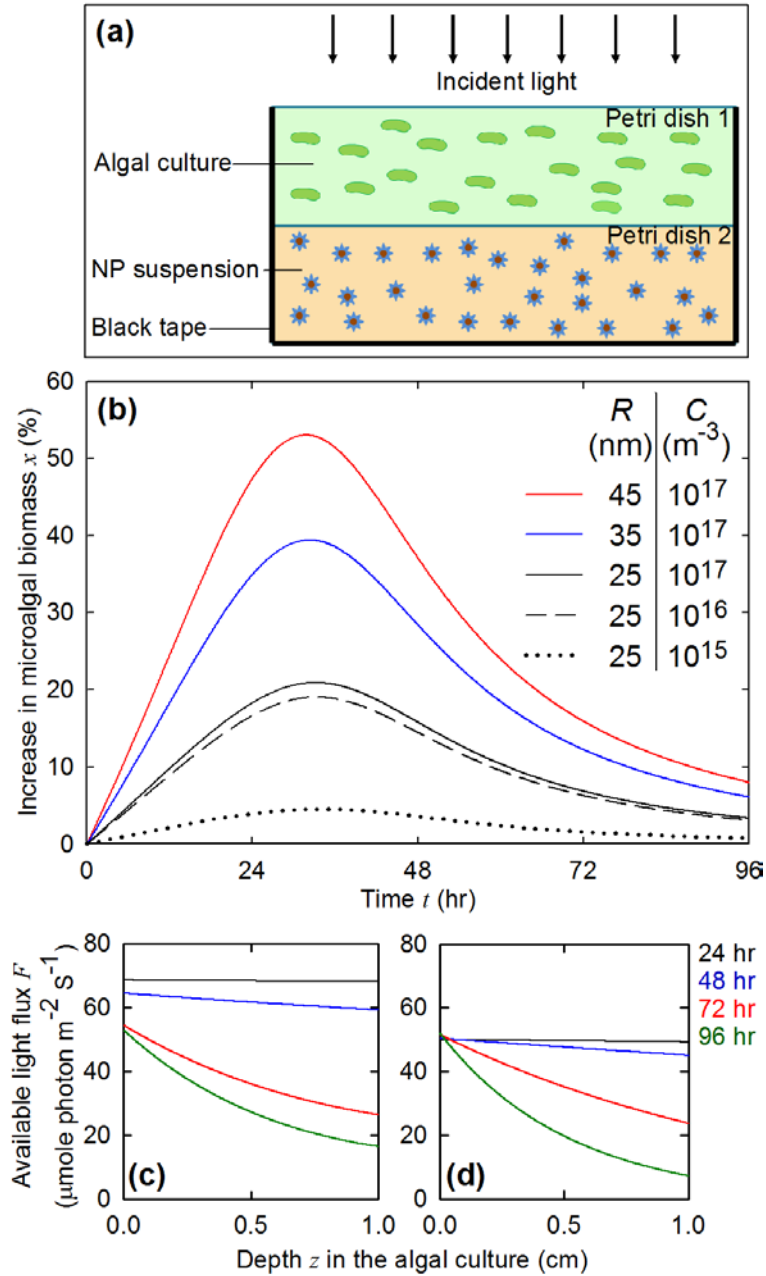
Figure 4.2: (a) schematic of the PMPBR, (b) the calculated effect of spherical Ag NP radius R and number density C on the relative biomass increase x for *Chlamydomonas reinhardtii* (c) the available irradiance $F(z, t)$ in the microalgae compartment for t = 24, 48, 72 and 96 hr (from top to bottom) for $C=10^{16}$ m^{-3} and R=45 nm and (d) corresponding scenario for the control which has no backscattering device. Source irradiance: 50 μ mol photon m^{-2} S^{-1}, MA culture and NP suspension depths: 1 cm each, the initial biomass concentration: 0.007 g L^{-1}.

Model predictions reported in Figures 4.2b-d clearly show that the presence of backscattering from the NP suspension increases the available flux and hence the relative biomass. Enhancement in the light flux obtained by increasing NP concentration or scattering cross-section promotes biomass growth. However, wavelength specificity diminishes for NPs because of multipole excitations [3]. The largest increase in the scattered light intensity in the blue region of the spectrum occurs for Ag NPs with radius of approximately 25 nm (Fig. 4.1). Note that the attenuation of light in the algal culture increases with increase in the biomass concentration. When growth reaches the late exponential phase (≈30 hours), the light flux available to MA becomes l imited, hence the plasmon-enhanced growth is also reduced. The model indicates that plasmon-enhancement becomes less effective when the culture depth is increased beyond 1 cm.

4.3   Experimental Method and Results

Experiments were conducted to study the growth of *Chlamydomonas reinhardtii* (green alga) and *Cyanothece 51142* (green-blue alga) in a PMPBR. The laboratory design of the PMPBR consisted of transparent cylindrical Petri dish (VWR #25364-090) containing the MA placed on top of that containing the NP suspension (Fig. 4.2a). The entire external surface except the top of the PMPBR was covered with black tape such that the incoming light could only enter from the top of the MA compartment. A fresh MA culture was inoculated into the PMPBR for each experiment. The initial biomass concentration of *Chlamydomonas* and *Cyanothece* was set to ~0.2 g L^{-1} and ~0.1 g L^{-1} respectively. The medium for *Chlamydomonas* was a minimum medium enriched with 20 mM $NaHCO_3$ [30],[29]. The ASP2 medium was used for *Cyanothece* [31],[32]. The NP suspensions were prepared by diluting a 10 wt%

NP/ethylene glycol suspension (Sigma-Aldrich) with water to obtain number densities 10^{15}, 10^{16} and 10^{17} m^{-3}. Average NP size was approximately 50 nm. The individual volumes of the MA culture and NP suspension in the PMBPR were 10 ml. Incident irradiance was kept at 50 μ mol photon m^{-2} S^{-1} and the temperature at 25°C and 30°C for *Chlamydomonas* and *Cyanothece* respectively. The cultures were grown over 96 hours without shaking. The biomass concentration was measured by its optical density (675 nm and 730 nm probes were used for *Chlamydomonas* and *Cyanothece* respectively).

It was inferred from figs. 4.3a-c that using the Ag NP suspension as a means for wavelength-specific backscattering leads to increase in microalgal growth in both species by more than 30%. The peak in the biomass growth manifests at later times (t ≈ 72 hr). The experimental data for plasmon-enhanced biomass growth is *qualitatively* consistent with the model predictions reported in fig. 4.2b. The quantitative disparity could be attributed to several factors: (1) the kinetics parameters we used in obtaining the theoretical predictions are based on growth data obtained from a large scale well-mixed PBR [29], which is likely to have different growth kinetics from the unstirred mini-size PMPBR employed in the present experiments, (2) the growth kinetics of MA contains an apparent lag phase which is not included in the model, (3) commercially available NPs may have non-uniform size and shape, which is inconsistent with model assumption of monodisperse spherical NPs and thus could alter the plasmonic response, and (4) the initial biomass concentration used in the experiments is much higher than that in the model since a critical initial biomass concentration is necessary to induce growth.
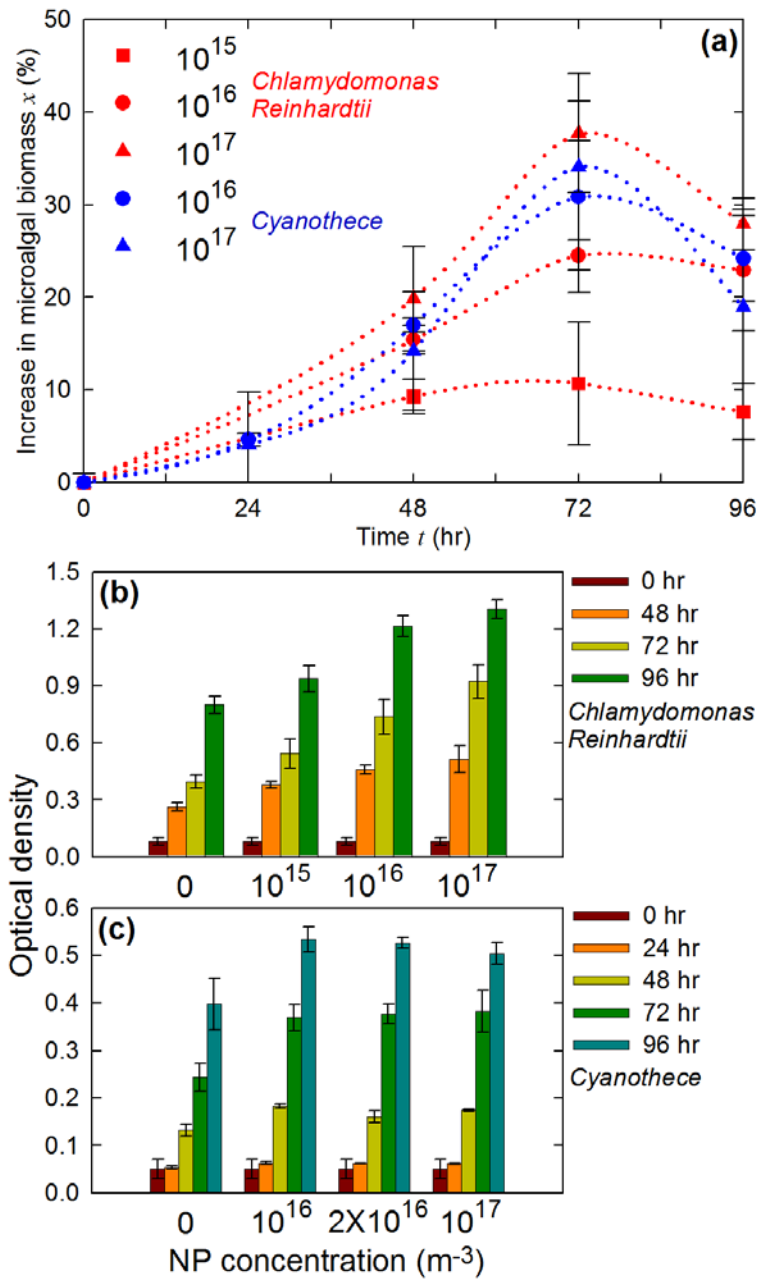
Figure 4.3: (a) Experimentally observed increase in microalgal biomass for *Cyanothece* **(NP concentrations: 10^{17} m^{-3} (▲) and 10^{16} m^{-3} (●)) and** *Chlamydomonas reinhardtii (***NP concentrations: 10^{17} m^{-3} (▲), 10^{16} m^{-3} (●) and 10^{15} m^{-3} (■)) with Ag NP suspension (R = 25 nm), Growth pattern of** *Chlamydomonas reinhardtii* **(b) and** *Cyanothece* **(c) for varying NP concentrations. Zero represents the control sample without the backscattering device.**

4.4 Effect of Nanoparticle Size and Architecture on Plasmonic Response

The size and architecture of plasmonic NPs can be used to tune the spectral response [2], specifically, Ag based NPs can be tuned to scatter light in blue and red regions of the EM spectrum where the microalga *Chlamydomonas reinhardtii* is most photoactive. We explore this idea theoretically by calculating and comparing plasmon responses of spherical, prolate ellipsoid and core (SiO$_2$)-shell (Ag) composite Ag NPs of various sizes suspended in water with the absroption spectrum of *Chlamydomonas reinhardtii* as show in figs. 4.4-6 respectively. The extinction efficiencies for the NPs were calculated with Mie theory. Note that Mie theory only completely describes extinction by spherical NPs. The quasi-static (point dipole) approximation with anisotropic depolarization factors was therefore used to describe the response of prolate ellipsoid NPs (assumed mono-disperse and randomly oriented in a suspension) [3].
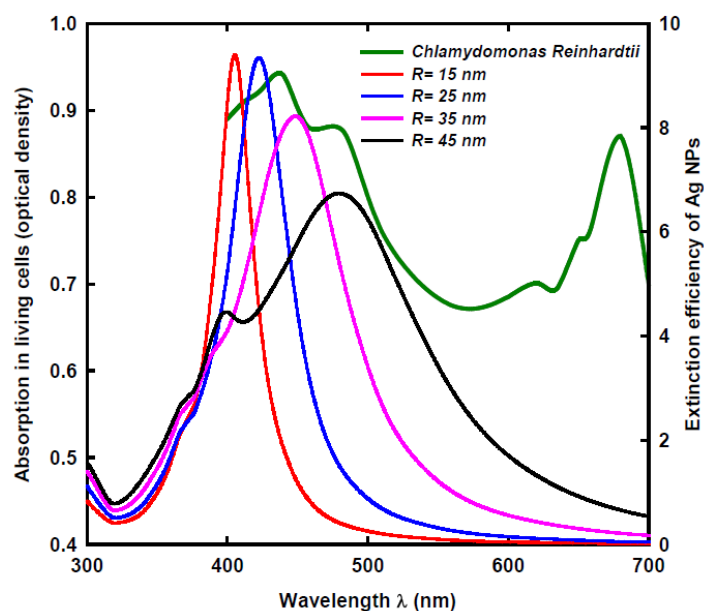
Figure 4.4: Plasmonic response spectra of spherical Ag NPs of various radii *R* suspended in water compared to the absorption spectrum of microalga *Chlamydomonas reinhardtii*. Notice the red-shift and loss in the sharpness of the peak for increasing NP radius. *R* ~ 25 nm gives highest peak.
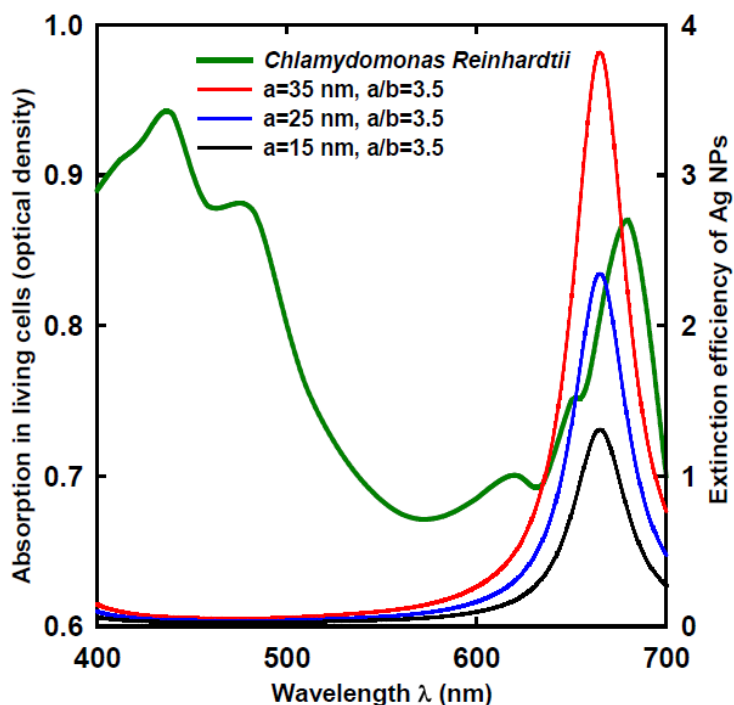
Figure 4.5: Plasmonic response spectra of prolate ellipsoidal Ag NPs of various major radii *a* and fixed eccentricity *a/b* compared to the absorption spectrum of microalga *Chlamydomonas reinhardtii*. Eccentricity induces a large red-shift in the plasmonic response leading to scattering in the red region of the spectrum (600-700 nm). Eccentricity *a/b* = 3.5 gives a good matching.

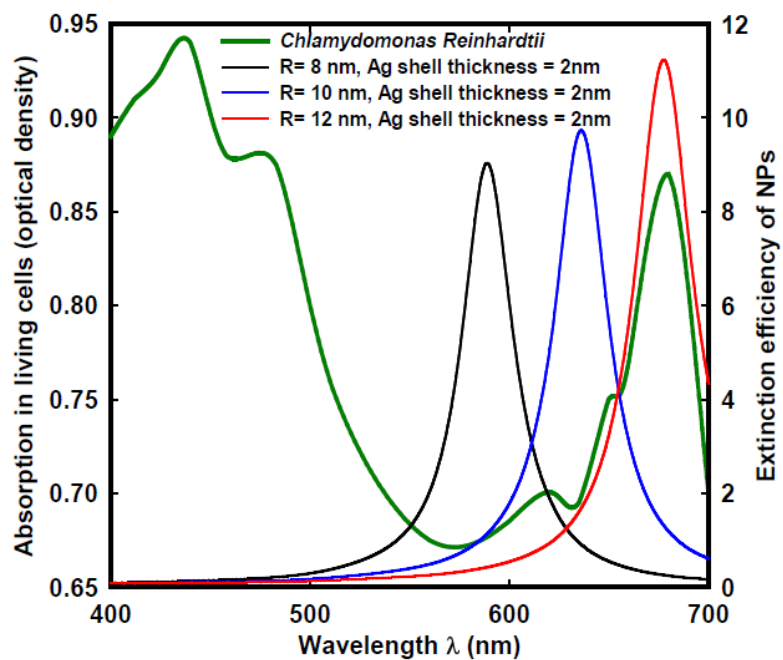**Figure 4.6: Plasmonic response spectra of SiO$_2$ core-Ag shell composite NPs with varying core radii *R* compared to the absorption spectrum of microalga *Chlamydomonas reinhardtii*. Presence of a dielectric core also induces a large red-shift in comparison to spherical Ag NPs making them usefull in the red region of the spectrum (600-700 nm). *R* ~ 12 nm gives a good matching.**

Chapter 5

Conclusion and Directions for Future Work

The FDTD method was adapted for the prediction of optical response of plasmonic composites for application to solar energy absorption in the visible region of the electromagnetic spectrum. Fair agreement was obtained with experimental data and theoretical models. Spectral spread of absorption was found to increase with the addition of multiple plasmonically active nanoparticles in the composite. This was found to be a beneficial route to covering the visible region of the solar spectrum between 300 and 800 nm. Especially, the incorporation of Ag and Cu into the composites led to absorption in most of the visible region. Effective medium theories were found most suitable in case of small particles and small volume fractions. Current simulations were limited by available computational power. In the future, more accurate simulations with custom built software could be used for more accurate predictions. Further, emergent non-linear properties of high volume fraction graded multi-metal composites could be explored with a possibility of getting closer to a perfect absorber response in the solar or any other application driven region of the electromagnetic spectrum.

It was also demonstrated that the use of plasmonic NP suspensions as wavelength specific backscattering devices in miniature PBRs could significantly promote the growth of photosynthetic microorganisms. In the experiments, the faster growth was facilitated by

enhancing the available irradiance in the blue region of the EM spectrum. However, optimal microalgal growth required light in two spectral regions, namely blue and red. It is impractical to mimic this bimodal behavior using a single NP species. In the present experiments, Ag NPs were selected for scattering blue light because it contains higher light energy under constant photon flux. However, backscattering in the red region (600-700 nm) can be facilitated by using prolate ellipsoids or composite core-shell spheres [2]. Hence, it is plausible that suitable mixtures of NPs, e.g. spheres and prolate ellipsoids, could be utilized to produce backscattering in both blue and red regions of the spectrum to achieve higher biomass growth rates. This is demonstrated in figs. 4. 3-5. Since the NP suspensions were confined and not dispersed within the culture medium, they can be used safely multiple times, thereby enabling the recovery of the additional material cost over a finite period of time. This observation motivates further explorations of practical and environmentally safe implementations of plasmon-enhanced biomass growth in small scale systems that could be used as biosensors as well as large scale applications aimed at harvesting algal biomass for the sustainable production of fuels and chemicals

References

[1] H.A. Atwater and A. Polman, "Plasmonics for improved photovoltaic devices," *Nature Mater.*, vol. 9, 2010, pp. 205-213.

[2] M.L. Brongersma and P.G. Kik, Eds., *Surface Plasmon Nanophotonics*, Dordrecht, Netherlands: Springer, 2007.

[3] C.F. Bohren and D.R. Huffman, *Absorption and Scattering of Light by Small Particles*, Hoboken, N. J.: Wiley-Interscience, 1998.

[4] S. Pillai, K.R. Catchpole, T. Trupke, and M.A. Green, "Surface plasmon enhanced silicon solar cells," *J. App. Phys.*, vol. 101, 2007, p. 09315.

[5] J. Trice, C. Favazza, R. Sureshkumar, H. Garcia, and R. Kalyanaraman, "Design and optimization of plasmonic-based metal-dielectric nanocomposite materials for energy applications," *Nanophotonic Materials V*, Z. Gaburro, S. Cabrini, and D. Talapin, Eds., San Diego, CA, USA: SPIE, 2008, pp. 70300M-13.

[6] H. Garcia, J. Trice, R. Kalyanaraman, and R. Sureshkumar, "Self-consistent determination of plasmonic resonances in ternary nanocomposites," *Phys. Rev. B*, vol. 75, 2007, p. 045439.

[7] M.A. Green, *Third Generation Photovoltaics: Advanced Solar Energy Conversion*, Springer, 2005.

[8] E. Hecht, *Optics*, Addison Wesley, 2001.

[9] J. Xi, M.F. Schubert, J.K. Kim, E.F. Schubert, M. Chen, S. Lin, W. Liu, and J.A. Smart, "Optical thin-film materials with low refractive index for broadband elimination of Fresnel reflection," *Nat. Photon.*, vol. 1, Mar. 2007, pp. 176-179.

[10] D.M. Trotter Jr. and A.J. Sievers, "Spectral selectivity of high-temperature solar absorbers," *Appl. Optic.*, vol. 19, 1980, pp. 711-728.

[11] S. Zhao and E. Wackelgard, "Optimization of solar absorbing three-layer coatings," *Sol. Energy Mater. Sol. Cells*, vol. 90, Feb. 2006, pp. 243-261.

[12] X. Li, Y. Chen, J. Miao, P. Zhou, Y. Zheng, and L. Chen, "High solar absorption of a multilayered thin film structure," *Optic. Express*, vol. 15, 2007, pp. 1907-1912.

[13] A. Taflove and S.C. Hagness, *Computational Electrodynamics: The Finite-Difference Time-Domain Method*, Artech House Publishers, 2005.

[14] E.F.C. Dreissen and M.J.A. de Dood, "The perfect absorber," *Appl. Phys. Lett.*, vol. 94, 2009, p. 171109.

[15] A. Sihvola, *Electromagnetic Mixing Formulae*, 2000.

[16] J.C. Maxwell-Garnett, "Colours in Metal Glasses and Metallic films," *Philos. Trans. R. Soc. London*, vol. 203, 1904, pp. 385-420.

[17] "SOPRALAB n-k database, http://www.sopra-sa.com/index2.php?goto=dl&rub=4."

[18] R.H. Magruder III, D.H. Osborne Jr., and R.A. Zuhr, "Non-linear optical properties of nanometer dimension Ag-Cu particles in silica formed by sequential ion implantation," *J. Non-Cryst. Solids*, vol. 176, 1994, pp. 299-306.

[19] L. Pottier, J. Pruvost, J. Deremetz, J. Cornet, J. Legrand, and C.G. Dussap, "A fully predictive model for one-dimensional light attenuation by Chlamydomonas reinhardtii in a torus photobioreactor," *Biotechnol. Bioeng.*, vol. 91, 2005, p. 571.

[20] D. Voet, J.G. Voet, and C.W. Pratt, *Fundamentals of Biochemistry*, Hoboken, N. J.: Wiley, 2008.

[21] G. Agel, W. Nultsch, and E. Rhiel, "Photoinhibition and its wavelength dependence in the cyanobacterium Anabaena variabilis," *Arch. Microbiol.*, vol. 147, 1987, p. 370.

[22] W. Nultsch, J. Pfau, and M. Materna-Weide, "Fluence and wavelength dependence of photomhibition in the brown alga Dictyota dichotoma," *Mar. Ecol. Prog. Ser.*, vol. 41, 1987, p. 93.

[23] J. Cornet, "Calculation of optimal design and ideal productivities of volumetrically lightened photobioreactors using the constructal approach," *Chem. Eng. Sci.*, vol. 65, 2010, p. 985.

[24] C.G. Lee and B.O. Palsson, "High-density algal photobioreactors using light-emitting diodes," *Biotechnol. Bioeng.*, vol. 44, 1994, p. 1161.

[25] H. Guedri and C. Durrieu, "A self-assembled monolayers based conductometric algal whole cell biosensor for water monitoring," *Microchimica Acta*, vol. 163, 2008, p. 179.

[26] M. Naessens and C. Tran-Minh, "Biosensor using immobilized Chlorella microalgae for determination of volatile organic compounds," *Sens. Actuators B*, vol. 59, 1999, p. 100.

[27] E. Pena-Vaszquez, E. Maneiro, C. Perez-Conde, M. Monero-Bondi, and E. Costas, "Microalgae fiber optic biosensors for herbicide monitoring using sol–gel technology," *Biosens. Bioelectron.*, vol. 24, 2009, p. 3538.

[28] J. Cornet, C.G. Dussap, and G. Dubertret, "A structured model for simulation of cultures of the cyanobacterium Spirulina platensis in photobioreactors: II. Identification of kinetic parameters under light and mineral limitations," *Biotechnol. Bioeng.*, vol. 40, 1992, p. 817.

[29] S. Fouchard, J. Pruvost, B. Degrenne, M. Titica, and J. Legrand, "Kinetic modeling of light limitation and sulfur deprivation effects in the induction of hydrogen production with Chlamydomonas reinhardtii: Part I. Model development and parameter identification," *Biotechnol. Bioeng.*, vol. 102, 2009, p. 232.

[30] M.V. Rajam and S.V. Kumar, "Agrobacterium Protocols," *Methods in Molecular Biology, vol. 344*:, K. Wang, Ed., Totowa, N. J.: Humana Press, 2007.

[31] K.J. Reddy, J.B. Haskell, D.M. Sherman, and L.A. Sherman, "Unicellular, aerobic nitrogen-fixing cyanobacteria of the genus Cyanothece," *J. Bacteriol.*, vol. 175, 1993, p. 1284.

[32] B. Wu, B. Zhang, X. Feng, J.R. Rubens, R. Huang, L.M. Hicks, H.B. Pakrasi, and Y.J. Tang, "Alternative isoleucine synthesis pathway in cyanobacterial species," *Microbiology*, vol. 156, 2010, p. 596.

Vita

Satvik Navinbhai Wani

Date of Birth	April 10, 1983
Place of Birth	Ahmedabad, India
Degrees	B.Tech. Metallurgical Engineering and Materials Science, June 2006 M Tech. Metallurgical Engineering and Materials Science, June 2006 M.S. Energy, Environmental and Chemical Engineering, August 2010
Professional Experience	Applications Engineer, KLA-Tencor India Pvt. Ltd., Chennai, India July 2006-Feb2007
Professional Societies	American Physical Society American Institute of Chemical Engineers
Publications	S. Torkamani, S. N. Wani, Y. J. Tang and R. Sureshkumar, "Plasmon-enhanced microalgal growth in miniphotobioreactors," *Appl. Phys. Lett.*, vol. 97, 2010, p. 043703

August 2010